

Real-Time LiDAR Point Cloud Compression and Transmission for Resource-constrained Robots

Yuhao Cao, Yu Wang and Haoyao Chen, *Senior Member, IEEE*

Abstract—LiDARs are widely used in autonomous robots due to their ability to provide accurate environment structural information. However, the large size of point clouds poses challenges in terms of data storage and transmission. In this paper, we propose a novel point cloud compression and transmission framework for resource-constrained robotic applications, called RCPCC. We iteratively fit the surface of point clouds with a similar range value and eliminate redundancy through their spatial relationships. Then, we use Shape-adaptive DCT (SA-DCT) to transform the unfit points and reduce the data volume by quantizing the transformed coefficients. We design an adaptive bitrate control strategy based on QoE as the optimization goal to control the quality of the transmitted point cloud. Experiments show that our framework achieves compression rates of $40\times$ to $80\times$ while maintaining high accuracy for downstream applications. Our method significantly outperforms other baselines in terms of accuracy when the compression rate exceeds $70\times$. Furthermore, in situations of reduced communication bandwidth, our adaptive bitrate control strategy demonstrates significant QoE improvements. The code will be available at <https://github.com/HITSZ-NRSL/RCPCC.git>.

I. INTRODUCTION

Field robots are typically equipped with LiDAR to perceive the surrounding environment and generate high-precision structural information. This information is utilized for spatial perception tasks such as object detection and 3D reconstruction. However, these tasks are often constrained by the limited computational resources of field robots, especially in scenarios that require real-time processing. To address this issue, as shown in Fig. 1, the combination of edge computing and cloud computing provides a feasible solution, by transmitting point cloud data to remote servers or the clouds to perform computationally intensive tasks. However, the vast amount of data generated by LiDAR, often reaching millions of points per second, presents a technical challenge for real-time transmission. Moreover, communication links in field environments are often unstable, and bandwidth is limited, further exacerbating the difficulty of data transmission. Therefore, how to achieve efficient point cloud compression and transmission under limited computing and communication resources remains a critical challenge.

Previous research has primarily focused on compression rate and point-to-point accuracy [1]–[3], but many of these methods are difficult to apply to resource-constrained robots

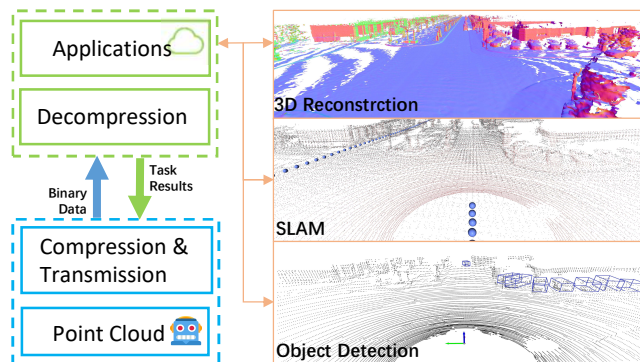


Fig. 1. A cloud service solution diagram for resource-constrained robots (left). And the downstream tasks results using the compressed point cloud (right).

due to their lack of real-time performance or reliance on heavy computation (e.g., requiring GPUs). Our work focuses on improving compression rate, compression speed, and application-level accuracy (e.g., for odometry and object detection). To ensure low end-to-end latency for applications, we introduce online control of compression quality, ensuring low latency and stability throughout the point cloud transmission pipeline.

We propose a real-time LiDAR point cloud compression and transmission framework for resource-constrained robots, named RCPCC, which achieves a high compression rate, maintains high application-level accuracy, and operates at a speed (>10 Hz) that exceeds the LiDAR point cloud generation rate, enabling computationally constrained robots to offload computation-intensive tasks to the cloud. To address bandwidth limitations and fluctuations during transmission, we propose a QoE-based adaptive bitrate control strategy that adjusts the transmission quality based on the current and historical buffer queue lengths, ensuring optimal QoE and guaranteeing real-time and stable point cloud transmission.

Our compression method uses range images as the basic representation of point clouds. Range images utilize the inherent physical properties of LiDAR, projecting 3D point clouds into 2D images, enabling high computational efficiency for subsequent processing. We iteratively fit surface models to the point clouds, fully leveraging the spatial characteristics of range images for point cloud encoding. For points not fitted by the surface model, we apply Shape-adaptive Discrete Cosine Transform (SA-DCT) [4] to the unfit points, avoiding zero-value noise artifacts [5] and achieving further compression.

The authors are with the School of Mechanical Engineering and Automation, Harbin Institute of Technology Shenzhen, P.R. China. 19B953030@stu.hit.edu.cn.

This work was supported in part by the National Natural Science Foundation of China under Grant U21A20119, as well as the Shenzhen Science and Innovation Committee under Grant RCJC20231211090050082 and Grant JCYJ20241202123714019. (Corresponding author: Yu Wang)

The main contributions of this paper are three-fold:

- A novel LiDAR point cloud compression and transmission framework, named RCPCC, is proposed to handle bandwidth fluctuations and enhance the real-time performance and stability of point cloud transmission.
- An adaptive bitrate control strategy based on QoE is proposed to handle bandwidth fluctuations and improve the real-time performance and stability of point cloud transmission.
- Extensive experiments demonstrate that, compared to state-of-the-art methods, RCPCC achieves a competitive compression rate and high accuracy while significantly reducing transmission latency.

II. RELATED WORKS

In this section, we review the research status of point cloud compression and transmission from the perspective of point cloud encoding and adaptive bitrate streaming.

A. Unstructured Point Cloud Encoding

Over the past few decades, significant progress has been made in point cloud compression. However, not all point cloud compression techniques are suitable for LiDAR point clouds. LiDAR point clouds have unique characteristics, such as sparsity, large coverage areas, and uneven density, making many compression methods designed for 3D object point clouds less effective. The most common and widely used methods for unstructured point cloud compression are based on spatial subdivision trees, such as octrees. These methods [6] [7] [8] [9] first use octrees as the foundational data structure to structure the point clouds, then apply various transformations and encoding schemes to reduce spatial and informational redundancy. In addition to octrees, clustering-based and segmentation-based methods [10] [11] have also demonstrated effectiveness in lossy geometric compression. To better capture geometric patterns, neural network-based methods [12] [13] learn the latent spatial structure and geometric information within the data, achieving superior lossy and lossless compression. However, these methods typically lack real-time capabilities and computational efficiency. Despite their effectiveness in many scenarios, the intrinsic physical properties of LiDAR sensors make LiDAR point clouds structured, and unstructured methods fail to take full advantage of this.

B. Structured Point Cloud Encoding

In structured point cloud compression, many works [14] project point clouds into 2D images for compression. Houshiar et al. [1] used panoramic cylindrical projections to convert point clouds into 2D images for lossless and JPEG lossy compression. Some works, such as the MPEG V-PCC framework, establish local reference frames on point cloud surfaces and generate orthogonal projection images from multiple views [15] [16]. These projection images are further compressed using existing image or video compression techniques. However, image or video compression methods like JPEG or H.265 are typically designed for rectangular

data with values between 0 and 255, without invalid pixels. Direct application to range images can introduce significant quantization errors and noise [17], leading to a reduction in downstream application accuracy.

C. Adaptive Bitrate Streaming

Common adaptive bitrate (ABR) schemes are crucial for video streaming [18]. They allow video streams to dynamically adjust video quality according to user network conditions, thereby avoiding video stuttering caused by network fluctuations. ABR methods aim to optimize Quality of Experience (QoE) by making optimal decisions. ABR methods can be broadly categorized into rate-based [19], buffer-based [20], hybrid [21], and RL-based [22] approaches. Some researchers have explored ABR for point cloud data transmission [23] [24]. Unfortunately, these methods were designed for dense 3D object point clouds and cannot be directly applied to LiDAR point clouds.

III. METHODOLOGY

A. System Overview

The proposed real-time LiDAR point cloud compression and transmission framework for resource-constrained scenarios, RCPCC, is illustrated in Fig. 2. Point clouds are first projected into range images using spherical coordinates. Subsequently, the range image is divided into macroblocks, and surface model fitting is performed on each macroblock. Points in fitted macroblocks are encoded and parameterized, while the fitted points are removed from the range image. For the unfit points, SA-DCT is applied to transform the data and quantize the transformed coefficients, balancing compression rate and quality. The adaptive bitrate control strategy uses the compression level and data queue length as input, adjusting the compression level for the next point cloud frame. Decoding is the inverse process of compression, allowing the original point cloud to be reconstructed using the corresponding inverse transforms.

B. Point Cloud Encoding

1) *Range Image Conversion*: LiDAR sensors typically represent point clouds in Cartesian coordinates relative to the sensor origin, denoted as (x, y, z) . Spherical projection maps the point cloud from Cartesian coordinates into spherical coordinates, generating a 2D panoramic range image, denoted as \mathcal{P} . The formula for spherical projection from the original point cloud to a 2D range image is as follows:

$$\begin{aligned} i &= \lfloor (\text{atan2}(y, x) + h_{offset}) / \Delta\theta \rfloor, \\ j &= \lfloor (\text{atan2}(z, \sqrt{x^2 + y^2}) + v_{offset}) / \Delta\varphi \rfloor, \\ r &= \sqrt{x^2 + y^2 + z^2}, \end{aligned} \quad (1)$$

where indices i and j represent the pixel coordinates in the range image, and r is the radial distance of the point cloud, which corresponds to the range value at (i, j) . h_{offset} and v_{offset} are horizontal and vertical offsets, respectively, related to the LiDAR's field of view (FOV), ensuring that i, j are non-negative. $\Delta\theta$ and $\Delta\varphi$ represent the discretization

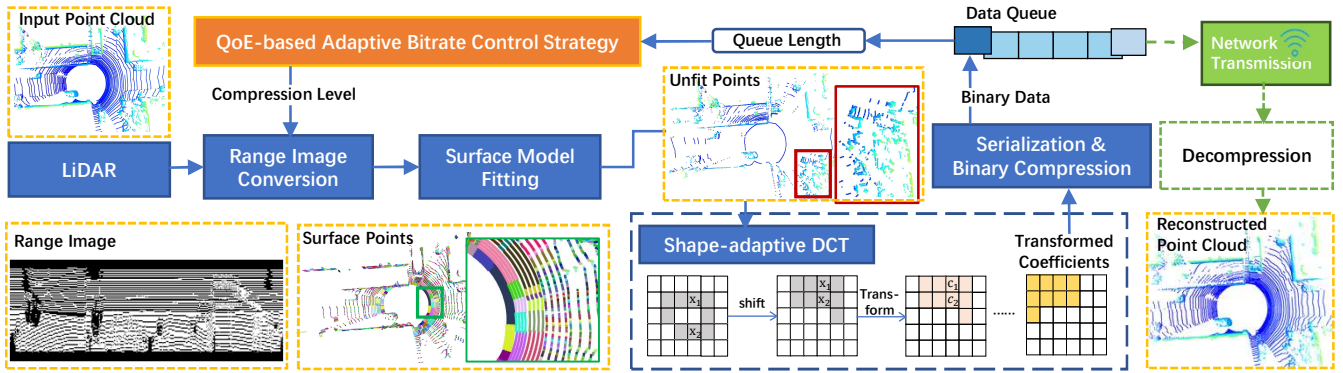


Fig. 2. Overview of the proposed *RCPC* framework. The input point cloud is first converted into a range image to accelerate the compression process. We use surface model fitting to eliminate spatial redundancy in the point cloud. Unfit points are transformed from the time domain to the frequency domain using SA-DCT, and the transformed results are quantized. Finally, all data required for decompression is serialized and fed into the binary entropy encoder.

granularity, depending on the horizontal and vertical resolution of the selected LiDAR. $\lfloor \cdot \rfloor$ represents the floor function.

The range image is a compact representation that allows the simplification of 3D point cloud operations into 2D image operations, improving computational efficiency. Additionally, neighboring points in the range image are more likely to belong to the same range surface, enabling better exploitation of spatial relationships for encoding.

2) *Surface Encoding*: In practice, point cloud compression will choose an appropriate spatial modeling method (e.g., using planes or points [11]) to extract the structural information of point clusters, reducing spatial redundancy. In fact, many points in real-world point clouds are located on the same plane (e.g., ground or walls), allowing these point clouds to be approximated by planes. A point cloud in the range image can be represented as $p_{i,j,r} = (i, j, r)$, and its Cartesian coordinates can be written as:

$$p_{x,y,z} = (r \cdot \cos \varphi \cdot \cos \theta, r \cdot \cos \varphi \cdot \sin \theta, r \cdot \sin \varphi), \quad (2)$$

where $\theta = i \cdot \Delta\varphi - h_{offset}$, and $\varphi = j \cdot \Delta\varphi - v_{offset}$ are the azimuth and elevation angles in the spherical coordinate system derived from the range image. The plane equation in Cartesian coordinates is given by $a \cdot x + b \cdot y + c \cdot z + d = 0$. We use the least squares method [25] to fit the plane on which the point cloud lies. Then, the plane model can be used to predict the radial range r of the point cloud. Given θ and φ , the predicted r value, denoted as \hat{r} , can be obtained using the following equation:

$$\hat{r} = -\frac{d}{a \cdot \cos \varphi \cdot \cos \theta + b \cdot \cos \varphi \cdot \sin \theta + c \cdot \sin \varphi}. \quad (3)$$

Previous works [11] [26] have employed such plane models, but the plane model is not the optimal choice since it cannot directly use (i, j) to predict \hat{r} without expensive trigonometric computations. A more intuitive method is to use Eq. 4, which we refer to as the surface model. Though the surface model is not a plane in Euclidean space, it better captures the spatial structure of points in the range image, and it is easier to compute:

$$\hat{r} = -\frac{d}{a \cdot i + b \cdot j + c}. \quad (4)$$

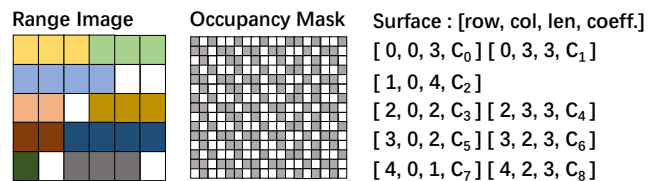


Fig. 3. The range image is divided into macroblocks, with different colors representing different surfaces (left). The occupancy mask marks the location of the point cloud in the range image, and the surface block is encoded using a four-tuple (right).

Inspired by this, as shown on the left side of Fig. 3, we divide the range image into macroblocks (e.g., 4×4) and iteratively fit the surface for each block. We set a distance threshold Δr . Only when all points in the block have distances to the surface less than Δr is the block considered a surface. For blocks in the same row, we use the surface parameters of the previous block to predict the next block and perform the Δr test. If the test passes, the blocks are merged and share the same surface parameters. To reconstruct the range image, as shown on the right side of Fig. 3, we record the positions of the point clouds in the range image as an occupancy mask, and we encode the surface using a four-tuple $(row, col, len, coefficients)$, recording the position and parameters of the surface block.

3) *Unfit Points Encoding*: After surface encoding, there will inevitably be some point clouds that are not fitted. The range image without all fitted surface points is called the unfit image. We can directly encode the original range values of unfit image, as in [26]. However, this will cause redundancy in accuracy because the surface model fitting has already relaxed the level of accuracy. Alternatively, it's a choice to use image encoding techniques (e.g., JPEG), but encoding the entire unfit image is not efficient as it contains a large number of zero-value pixels, which are redundant. Moreover, image compression may introduce zero-value noise [5].

To only encode the areas of interest without introducing zero-value noise, the Shape-Adaptive DCT (SA-DCT) is applied on the unfit image to perform temporal and frequency

domain transformations. The core concept of SA-DCT for compressing the unfit point cloud is shown in Fig. 2. During encoding, only the remaining unfit points in the unfit image are shifted to the upper edge of the column and undergo a 1D DCT transformation. The 1D DCT transformation on the column(row) vector \mathbf{x} produces the 1D vector \mathbf{c}_k as follows:

$$\mathbf{c}_k = A_{L_k} \cdot \mathcal{DCT}_{L_k} \cdot \mathbf{x}_k. \quad (5)$$

After that, the transformed non-zero elements are shifted to the left edge by rows, and a one-dimensional DCT transformation is performed. Finally, we obtain a coefficient matrix \mathcal{C} . The corresponding inverse transformation formula is as follows:

$$\mathbf{x}_k = \frac{2}{A_{L_k} L_k} \cdot \mathcal{DCT}_{L_k}^T \cdot \mathbf{c}_k, \quad (6)$$

where L_k is the length of the vector \mathbf{x} , A_{L_k} is the normalization factor, and the definition of \mathcal{DCT}_{L_k} is as follows:

$$\mathcal{DCT}_L(p, k) = a_0 \cdot \cos\left(p\left(k + \frac{1}{2}\right) \frac{\pi}{L_k}\right), \quad (7)$$

$$a_0 = \begin{cases} \sqrt{\frac{1}{2}}, & \text{if } p = 0 \\ 1, & \text{otherwise.} \end{cases}$$

After transformation, we quantize the coefficient matrix \mathcal{C} by the quantization step q_{step} to obtain the quantized coefficient matrix \mathcal{C}^* (* denotes the quantized result). Quantization introduces quantization errors but reduces the data size, increasing the compression rate of the entropy encoder [27]. During SA-IDCT reconstruction, the position of non-zero elements in the original data is needed for the inverse transform. However, no additional storage is required because the non-zero elements' positions can be derived from the occupancy mask by excluding the fitted points' mask.

C. QoE-based Adaptive Bitrate Control

In video streaming, ABR allows the video stream to dynamically adjust its quality based on network conditions, thus avoiding stuttering due to network fluctuations and improving the QoE [23]. For point cloud transmission used in cloud services, the server aims to receive small, high-quality point clouds from robots in real-time. We define a QoE objective function related to real-time transmission quality for cloud services, formulated as follows:

$$QoE = \sum_{i=1}^n q(R_i) - \mu \sum_{i=1}^n K_i - \sum_{i=1}^{n-1} |q(R_{i+1}) - q(R_i)| \quad (8)$$

in which the first term $q(\cdot)$ assigns a quality score based on compression level, and R_i represents the configuration parameter of the compression level used for the i -th frame point cloud compression, including vertical and horizontal resolution, surface threshold, quantization level. The second term serves as a penalty for the length of the buffer queue, where K_i represents the length of the buffer queue of the data packet encoded by the i -th frame point cloud waiting to be sent; μ is the corresponding weight. The third term

is a penalty for switching quality, which is utilized to avoid frequent quality switching.

By optimizing the (8), the compression level configuration throughout the entire transmission process $R_{i:N}^*$ can be solved as:

$$R_{i:N}^* = \arg \min_{R_{i:N}} QoE$$

$$s.t. \quad R_i \in \{C_1, C_2, \dots\}.$$

To address this online optimization problem, we propose a strategy based on the following schemes:

- **Quality improvement attempts:** If the queue remains stable over a long period, we attempt to improve the quality (the first term of QoE). If the result is not satisfactory, we revert to the previous state.
- **Historical memory:** Decisions are made not only based on the current state but also by considering the historical buffer length (related to the second term).
- **Buffer switching:** Quality switching does not immediately affect the buffer length. Hence, a buffer period is necessary between switches to reduce the penalty from frequent quality changes (reduce the third term).

These schemes form the basis of our QoE-based adaptive bitrate control strategy, which optimizes transmission quality while minimizing latency.

IV. EXPERIMENTS

A. Experimental Setup

The baseline point cloud compression methods selected for comparison are: the KDTree-based method from Google: Draco [9]; Geometry-based compression method: G-PCC [15], [16]; Range image-based compression using JPEG2000 (JPEG Range) [28]; the octree-based method from the Point Cloud Library (PCL) [29].

Our experiments were conducted on a desktop platform with an Intel i7-12650H processor and 16 GB of RAM. For localization [30], we used the LiDAR odometry KISS-ICP [31] on the KITTI odometry dataset [32]. For object detection, we used PointPillar [33] on the KITTI detection dataset. For mesh reconstruction, we used VDBFusion [34] to extract meshes via TSDf maps and marching cubes on the MaiCity dataset. To comprehensively evaluate performance, we tested all methods across all sequences and frames and calculated the arithmetic mean. Our method's parameters include $(\Delta\theta, \Delta\varphi, \Delta r, q_{step})$, and in subsequent experiments, we use a four-tuple to represent the parameter settings.

For QoE-based Adaptive Bitrate Control, we manually simulated network bandwidth variations using a local area network (LAN) router and recorded the compression quality and buffer queue length at each time step, computing the QoE for the entire transmission process.

B. Comparative Results

Mesh Reconstruction Our compression method outperformed other methods, achieving better mapping performance and higher compression ratios. we use the F-score to evaluate surface quality in mesh reconstruction and the

compression ratio is computed as original point cloud size divided by the final binary size.

Fig. 4 compares the F-scores of different methods at various compression ratios. Our method can achieve a compression ratio of $100.5\times$ and maintain an F-score of 95.94%. At a compression ratio of $198.4\times$, our method’s F-score remains at 91.70%. In comparison, the best-performing Draco achieved an F-score of 94.07% at a compression ratio of $100.7\times$, and as the compression ratio further increases, the performance of other methods’ F-scores drops rapidly, while our method still maintains a stable F-score performance. Our method effectively combines and balances quantization and down-sampling strategies, even at a very high compression ratio (even at $557\times$), it can still maintain a stable F-score.

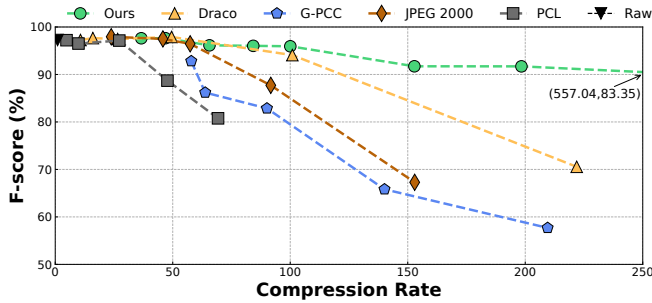


Fig. 4. The F-score of mesh reconstruction and compression rate comparison of various methods.

Localization Our compression method has an average translation error(%) [31] lower than other baseline methods when the compression ratio is greater than $100\times$. Fig. 5 shows the Translation Error(%) of different methods at different compression ratios on the KITTI dataset (seq.00~10). We did not show the results of the PCL because the PCL failed in this test. In Fig. 5, our method achieves $36.3\times$ compression rate while maintaining almost the same Translation Error (%) as the original point cloud. As the compression rate increases, our method’s localization performance remains stable, while JPEG2000 and Draco show a significant increase in Translation Error (%) to 4.29% and 9.62% at around $100\times$. In contrast, our method maintains a low error rate of 0.71% at a $99.7\times$ compression rate, outperforming all other baseline methods.

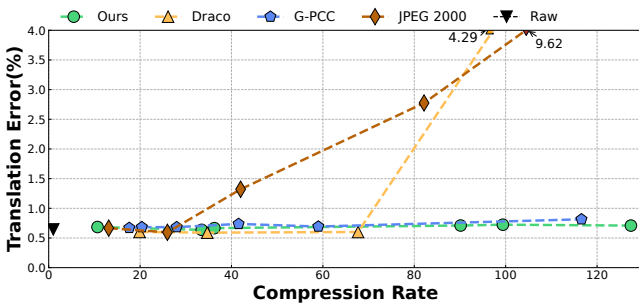


Fig. 5. Average translation error and compression rate comparison of various methods.

Object Detection Our method achieves higher object

detection accuracy than the other methods when the compression rate exceeds $36.4\times$. The overall bounding box average precision (AP) for annotated classes [33] is evaluated. Fig. 6 shows BBox AP(%) on the KITTI object detection dataset for different methods at various compression rates. Compared to the original point cloud’s 80.89% accuracy, our method achieves a competitive 79.03% accuracy at a compression rate of $14.4\times$. As the compression rate increases, our method maintains 68.8% accuracy at a compression rate of $41.4\times$. In contrast, PCL and JPEG2000’s accuracy drops rapidly, falling below 40% at compression rates greater than $40\times$.

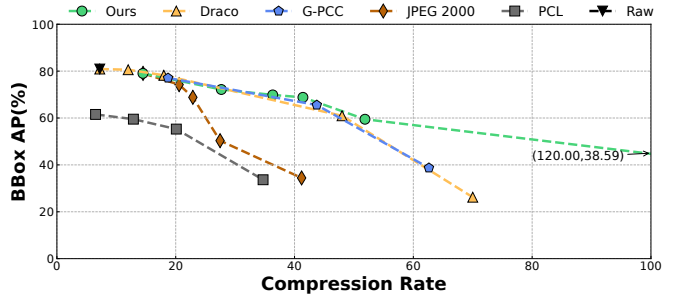


Fig. 6. The object detection BBox AP and compression rate comparison of various methods.

C. Ablation Study

To verify the impact of the modules mentioned earlier, we conducted experiments on 1,000 frames from the KITTI dataset and recorded the relevant data. All experiments were conducted with parameter settings (0.5, 0.5, ., .).

Plane Model and Surface Model. Tab.I shows the mean average error (MAE) of point clouds predicted by plane and surface models compared to the ground truth in the range image at various distance thresholds. Under the same distance threshold, surface models produce lower MAE than plane models.

SA-DCT Tab.II compares the MAE and corresponding compression rate between no compression of the unfit image (No Compr.) and compressing the unfit image using SA-DCT. With No Compr. (generated only by surface model fitting), the pipeline achieves $32.40\times$ compression rate with an MAE of 3.68. With SA-DCT, the compression rate improves to $40.86\times$ when the quantization step is 0.10, with a slight increase in MAE to 5.29. The experiments demonstrate that our method achieves a significant improvement in compression rate with an acceptable increase in error.

TABLE I
FITTED POINTS MAE COMPARISON BETWEEN PLANE MODEL AND SURFACE MODEL, MAE UNIT: *cm*.

Model	Plane			Surface		
Threshold	0.1m	0.3m	0.5m	0.1m	0.3m	0.5m
Fitted MAE	5.97	13.46	16.70	4.75	10.82	11.92

TABLE II

COMPARISON RESULTS OF USING SA-DCT ON UNFIT POINTS AND NO COMPRESSION. CR: COMPRESSION RATE, QS: QUANTIZATION STEP, MAE UNIT: cm .

Configuration	Unfit MAE	MAE	CR
No Compr	0.19	3.68	32.40
SA-DCT(0.10)	4.23	5.29	40.86
SA-DCT(0.40)	16.71	10.30	47.19
SA-DCT(1.00)	41.28	20.05	53.37

D. Transmission Experiments

For Transmission, we evaluate the QoE during point cloud transmission, which is critical for the quality of cloud services. We compare the transmission performance of our point cloud compression method with and without the strategy, where the compression level is predefined from fine to coarse (0 to 5) based on different parameters. In Fig. 7, the time points where the bandwidth changes are marked with vertical dashed lines. The experiment starts with a bandwidth of 300KB/s, which drops sharply to 100KB/s at 55 seconds (simulating interference or the robot entering a closed building where signal quality degrades); at 120 seconds, the bandwidth increases slightly to 130KB/s; and at 245 seconds, the bandwidth rises to 160KB/s (indicating that the robot has moved away from interference or exiting the closed building).

In Fig. 7, when the bandwidth decreases due to the buffer switching characteristic of our adaptive bitrate control strategy, the compression level gradually increases from 0 to 5 to adapt to the bandwidth change. As a comparison, the compression level of without strategy remains at 0 during bandwidth drops, causing the data queue to grow and eventually leading to increased transmission delays. When the bandwidth rises at 125 seconds, our strategy gradually lowers the compression level (through the quality improvement attempts) to provide higher-quality point clouds. However, this quality improvement can cause delays, and at 160 seconds, reducing the compression level to 0 results in an increased queue length. Our historical memory scheme prevents the overuse of the quality improvement attempts by rolling back the compression level, maintaining stability in the data queue.

To calculate QoE, we set the quality evaluation function as $q(i) = 25 - 5i, i \in \{0...5\}$ and $\mu = 0.5$. Throughout the point cloud transmission, the average QoE of the method with strategy is 18.33, while without strategy, the average QoE is 60.18. Our method maintains a shorter data queue length throughout transmission, reducing transmission delay.

E. Runtime Analysis

Tab. III compares the runtime of our method against other baseline methods. Our method's parameter settings are (0.5, 0.5, 0.3, 0.2), and all methods were set to achieve similar compression rates (approximately 60x). Our method's encoding time is 41.05 ms, and decoding time is 11.35 ms.

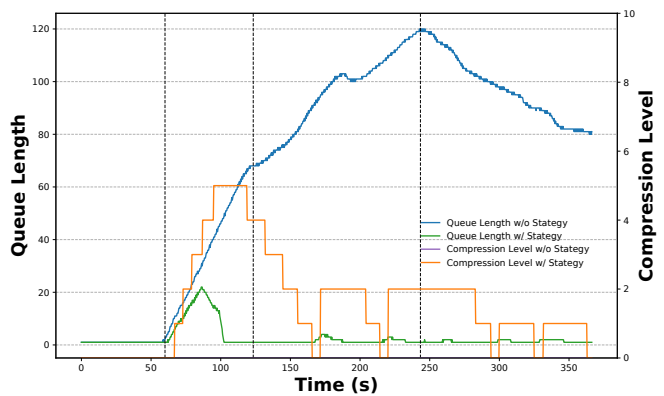


Fig. 7. Comparison of the experiment results for point cloud transmission with and without the QoE-based adaptive bitrate control strategy.

TABLE III

AVERAGE TIME CONSUMPTION (MS) OF DIFFERENT METHODS ON THE KITTI DATASET

Method	Encode (ms)	Decode (ms)	Total (ms)
G-PCC	445.41	238.93	684.34
Draco	49.08	10.68	59.76
JPEG	36.37	13.79	50.13
PCL	144.90	86.43	231.33
Ours	41.06	11.35	52.41

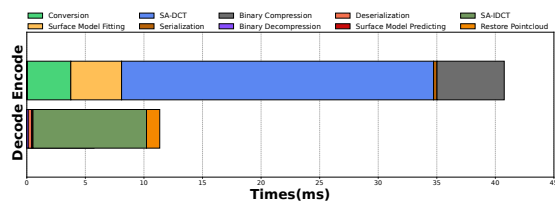


Fig. 8. The module runtime breakdown of our method.

The speed of our method is sufficient to support real-time point cloud compression for current LiDAR.

Fig. 8 provides a detailed runtime breakdown of our method's encoding and decoding processes. The most time-consuming components of the pipeline are SA-DCT and its inverse transformation.

V. CONCLUSIONS

This paper presents a novel real-time LiDAR point cloud compression and transmission framework, called *RCPC*. The combination of efficient point cloud compression and adaptive bitrate control strategy enables our method to help resource-constrained robots achieve real-time point cloud transmission. Our method achieves a compression rate of up to 80x, with real-time compression speed (> 10 FPS) while maintaining high application accuracy. It surpasses state-of-the-art point cloud compression standards in terms of compression rate, speed, and accuracy.

REFERENCES

- [1] H. Houshiar and A. Nüchter, "3d point cloud compression using conventional image compression for efficient data transmission," in *Proc. 25th Int. Conf. Inf., Commun. Autom. Technol.*, 2015, pp. 1–8.

- [2] S. Lasserre, D. Flynn, and S. Qu, "Using neighbouring nodes for the compression of octrees representing the geometry of point clouds," in *Proceedings of the 10th ACM Multimedia Systems Conference*, 2019, pp. 317–327.
- [3] C. Tu, E. Takeuchi, C. Miyajima, and K. Takeda, "Compressing continuous point cloud data using image compression methods," in *Proceedings of the 2016 IEEE/RSJ International Conference on Intelligent Robots and Systems (IROS)*, 2016, pp. 3935–3940.
- [4] T. Sikora, "Low complexity shape-adaptive dct for coding of arbitrarily shaped image segments," *Signal Processing: Image Communication*, vol. 7, no. 4-6, pp. 381–395, 1995.
- [5] M. Sun, X. He, S. Xiong, C. Ren, and X. Li, "Reduction of jpeg compression artifacts based on dct coefficients prediction," *Neurocomputing*, vol. 384, pp. 335–345, 2020.
- [6] J. Elseberg, D. Borrmann, and A. Nüchter, "One billion points in the cloud—an octree for efficient processing of 3d laser scans," *ISPRS Journal of Photogrammetry and Remote Sensing*, vol. 76, pp. 76–88, 2013.
- [7] P. de Oliveira Rente, C. Brites, J. Ascenso, and F. Pereira, "Graph-based static 3d point clouds geometry coding," *IEEE Transactions on Multimedia*, vol. 21, no. 2, pp. 284–299, 2018.
- [8] X. Zhang, W. Wan, and X. An, "Clustering and dct based color point cloud compression," *Journal of Signal Processing Systems*, vol. 86, no. 1, pp. 41–49, 2017.
- [9] R. L. de Queiroz and P. A. Chou, "Compression of 3d point clouds using a region-adaptive hierarchical transform," *IEEE Transactions on Image Processing*, vol. 25, no. 8, pp. 3947–3956, Aug. 2016.
- [10] T. Ochotta and D. Saupe, "Compression of point-based 3d models by shape-adaptive wavelet coding of multi-height fields," in *Proc. Symp. Point Based Graph.*, Zürich, Switzerland, Jun. 2004, pp. 103–112.
- [11] S. Wang, J. Jiao, P. Cai, and L. Wang, "R-pcc: A baseline for range image-based point cloud compression," in *2022 International Conference on Robotics and Automation (ICRA)*, Philadelphia, PA, USA, 2022.
- [12] C. Fu, G. Li, R. Song, W. Gao, and S. Liu, "Octattention: Octree-based large-scale contexts model for point cloud compression," in *Proceedings of the AAAI Conference on Artificial Intelligence*, vol. 36, no. 1, June 2022, pp. 625–633.
- [13] Y. He, X. Ren, D. Tang, Y. Zhang, X. Xue, and Y. Fu, "Density-preserving deep point cloud compression," in *Proceedings of the IEEE/CVF Conference on Computer Vision and Pattern Recognition*, 2022, pp. 2333–2342.
- [14] J. Heo, C. Phillips, and A. Gavrilovska, "Flicr: A fast and lightweight lidar point cloud compression based on lossy ri," in *2022 IEEE/ACM 7th Symposium on Edge Computing (SEC)*, Dec. 2022, pp. 54–67.
- [15] E. S. Jang, M. Preda, K. Mammou, A. M. Tourapis, J. Kim, D. B. Graziosi, S. Rhyu, and M. Budagavi, "Video-based point-cloud compression standard in mpeg: From evidence collection to committee draft [standards in a nutshell]," *IEEE Signal Processing Magazine*, 2019.
- [16] P. A. C. M. Krivokua and M. Koroteev, "A volumetric approach to point cloud compression part ii: Geometry compression," *IEEE Transactions on Image Processing*, 2020.
- [17] L. Zheng, K. Xu, J. Jiang, M. Wei, B. Zhou, and H. Cheng, "Real-time efficient environment compression and sharing for multi-robot cooperative systems," *IEEE Transactions on Intelligent Vehicles*, 2024.
- [18] A. Bentaleb, B. Taani, A. C. Begen, C. Timmerer, and R. Zimmermann, "A survey on bitrate adaptation schemes for streaming media over http," *IEEE Communications Surveys Tutorials*, vol. 21, no. 1, pp. 562–585, 2019.
- [19] J. Jiang, V. Sekar, and H. Zhang, "Improving fairness, efficiency, and stability in http-based adaptive video streaming with festive," in *Proc. ACM 8th Int. Conf. Emerg. Netw. Exp. Technol. (CoNEXT)*, 2012, pp. 97–108.
- [20] K. Spiteri, R. Urgaonkar, and R. K. Sitaraman, "Bola: Near-optimal bitrate adaptation for online videos," in *Proc. IEEE INFOCOM 35th Annu. Int. Conf. Comput. Commun.*, 2016, pp. 1–9.
- [21] X. Yin, A. Jindal, V. Sekar, and B. Sinopoli, "A control-theoretic approach for dynamic adaptive video streaming over http," *SIGCOMM Comput. Commun. Rev.*, vol. 45, no. 4, pp. 325–338, Aug. 2015.
- [22] A. Bentaleb, A. C. Begen, and R. Zimmermann, "Orl-sdn: Online reinforcement learning for sdn-enabled http adaptive streaming," *ACM Transactions on Multimedia Computing, Communications, and Applications*, vol. 14, no. 3, pp. 1–28, 2018.
- [23] L. Wang, C. Li, W. Dai, S. Li, J. Zou, and H. Xiong, "Qoe-driven adaptive streaming for point clouds," *IEEE Transactions on Multimedia*, vol. 25, pp. 2543–2558, 2022.
- [24] M. Hosseini and C. Timmerer, "Dynamic adaptive point cloud streaming," in *Proceedings of the 23rd Packet Video Workshop*, 2018, pp. 25–30.
- [25] P. Podulka, "Selection of reference plane by the least square fitting methods," *Advances in Science and Technology. Research Journal*, vol. 10, no. 30, pp. 164–175, 2016.
- [26] Y. Feng, S. Liu, and Y. Zhu, "Real-time spatio-temporal lidar point cloud compression," in *2020 IEEE/RSJ International Conference on Intelligent Robots and Systems (IROS)*, 2020, pp. 10766–10773.
- [27] Y. Collet and M. Kucherawy, "Zstandard compression and the application/zstd media type," 2018.
- [28] C. Christopoulos, A. Skodras, and T. Ebrahimi, "The jpeg2000 still image coding system: An overview," *IEEE Transactions on Consumer Electronics*, vol. 46, no. 4, pp. 1103–1127, 2000.
- [29] R. B. Rusu and S. Cousins, "3d is here: Point cloud library (pcl)," in *2011 IEEE international conference on robotics and automation*. IEEE, 2011, pp. 1–4.
- [30] J. Liu, G. Wang, C. Jiang, Z. Liu, and H. Wang, "Translo: A window-based masked point transformer framework for large-scale lidar odometry," in *Proceedings of the AAAI Conference on Artificial Intelligence*, vol. 37, no. 2, 2023, pp. 1683–1691.
- [31] I. Vizzo, T. Guadagnino, B. Mersch, L. Wiesmann, J. Behley, and C. Stachniss, "Kiss-icp: In defense of point-to-point icp—simple, accurate, and robust registration if done the right way," *IEEE Robotics and Automation Letters*, vol. 8, no. 2, pp. 1029–1036, 2023.
- [32] A. Geiger, P. Lenz, C. Stiller, and R. Urtasun, "Vision meets robotics: The kitti dataset," *The International Journal of Robotics Research*, vol. 32, no. 11, pp. 1231–1237, 2013.
- [33] A. H. Lang, S. Vora, H. Caesar, L. Zhou, J. Yang, and O. Beijbom, "Pointpillars: Fast encoders for object detection from point clouds," in *Proceedings of the IEEE/CVF conference on computer vision and pattern recognition*, 2019, pp. 12697–12705.
- [34] I. Vizzo, T. Guadagnino, J. Behley, and C. Stachniss, "Vdbfusion: Flexible and efficient tsdf integration of range sensor data," *Sensors*, vol. 22, no. 3, 2022. [Online]. Available: <https://www.mdpi.com/1424-8220/22/3/1296>